Phys. Rev. Lett. (2016) 116, 134501

Local slip length of superhydrophobic surfaces: distribution, anisotropy and effective slip

David Schäffel, Kaloian Koynov, Doris Vollmer, Hans-Jürgen Butt and Clarissa Schönecker*
Max Planck Institute for Polymer Research, Mainz, Germany
(Dated: September 14, 2015)

While the global slippage of water past superhydrophobic surfaces has attracted wide interest, the local distribution of slip still remains unclear. Using fluorescence correlation spectroscopy, we performed detailed measurements of the local slip length for water in the Cassie state on a microstructured superhydrophobic surface. We revealed that the local slip length is finite, non-constant, anisotropic and sensitive to the presence of surfactants. In combination with numerical calculations of the flow, we can explain all these properties by the local hydrodynamics.

The question whether and how a Newtonian fluid is able to slip over a solid surface has arisen with the development of theoretical models for fluid motion at the beginning of the 19th century. Due to its high fundamental and technological importance it has been continuously studied and controversially discussed ever since. Still, it is not yet fully answered. Following Navier [1], slippage is typically characterized by the slip length b, relating velocity u and stress at the surface via the boundary condition $u = b(\partial u/\partial n)$ with n being the normal to the surface. While the intrinsic slip on smooth, hydrophobic surfaces has been found to be below 50 nm [2–9], a fundamental understanding of the presumably much larger and therefore technologically much more relevant apparent slip on rough surfaces is still missing. This type of slip is due to a fluid being in the Cassie state, i.e. for typical superhydrophobic surfaces air is entrapped underneath the water in surface indentations. In this case, experiments are usually limited to a global investigation of the effective slip length or its effect on the flow [10–15]. Bolognesi et al. found the local slip length to be finite [16]. Still, an understanding of the local processes, like local slip length distribution or magnitude based on the surface design are not yet available. In theoretical calculations, the water-air interfaces are treated in a strongly idealized way, either as perfectly slipping without any resistance [17–23], with a constant local slip length [24, 25] or with a generic, isotropic distribution [26–28], although these properties have not yet been measured. Moreover, the underlying flow pattern of the air, the viscosity of the lubricant and the surface topography should lead to non-constant values of the local slip length [29]. For the physical understanding of slippage at superhydrophobic surfaces that would allow designing optimal surface properties it is essential to explore the microscopic details of the local slip length.

In this letter, we present an extensive study of the the underlying mechanisms of slippage at topographically structured, air-entrapping surfaces. We show that the local slip length has a non-constant, anisotropic distribution related to the flow pattern of the lubricating fluid and furthermore depends on surface-active substances

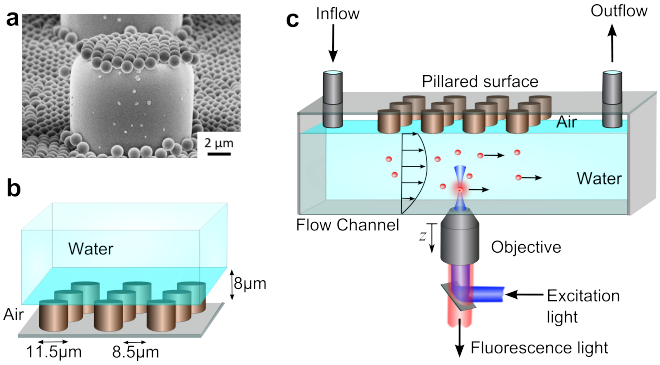

FIG. 1: (a): Scanning electron microscopy image of a pillar of the model surface; (b): Schematic representation of the surface topography; (c): Schematic of the experimental setup

adhering to the water-air interface. We obtain further insight into the physics of slippage by developing a numerical model that considers the local flow field of the entrapped air. Additionally, we discuss implications of our new findings on the currently accepted models.

As a model surface, we used a square pattern of pillars of 11.5 µm in diameter and a distance of 20 µm (fig. 1), prepared by photolithography of SU8-photoresist on a glass microscope slide and subsequent coating with 1.1 µm sized polystyrene beads and fluorinazation with 1H,1H,2H,2H-perfluorooctyltrichlorosilane [30]. The surface is superhydrophobic (static constact angle 160°), which is however not strictly needed for slippage. The essential feature is that water placed on the surface stays in the Cassie state and encloses air in between the pillars. The beads on the top faces ensure a stable Cassie state even under flow.

The structured surface constitutes the upper wall of a microchannel of 150 µm height, 4 mm width and 50 mm length (fig. 1(c), for details on the microchannel, see [31, 32] and Supplementary Information (SI)). Fluorescence Correlation Spectroscopy (FCS) [31, 33–38] was used to measure the flow and to deduce the slip length with a high local specificity. As tracers, we used Qdot 585 ITK^{TM} carboxyl quantum dots (Invitrogen) with a

hydrodynamic radius of $R_h = 6.3nm$. In order to prevent possible electrostatic repulsion of the quantum dots from the fluidic interfaces a 0.1 mM K_2HPO_4 solution (Sartorius Arium purified water) was used, corresponding to a Debye shielding length of $\lambda_D \approx 17\,\text{nm}$. Before applying this solution, the system was flushed with purified water for 30 min.

By using a hydrostatic pressure difference the solution was pumped through the microchannel at a flow rate of $35\,\text{mm}^3/\text{s}$. After ensuring a stable Cassie state, flow velocity profiles were collected with a combined FCS-confocal microscopy setup (Carl Zeiss (Germany), Axiovert 200 inverted microscope, LSM510 and ConfoCor2 modules, C-Apochromat 40x, NA 1.2 water-immersion objective). Starting from various positions at the air-water interface (fig. 2(a)), FCS autocorrelation curves were recorded and evaluated to yield the flow velocity at the respective position of the detection volume (for details, see SI). The exact position of the pillar-water and the air-water interface was determined for each velocity profile by the highest gradient in the measured fluorescence intensity, yielding a vertical accuracy of 0.3 µm. Because of the strong surface tension, the water-air interface remains relatively flat under flow, showing a maximum deflection at point (6|6) of <1 µm.

Typical profiles for the velocity u are shown in fig. 3. The local slip length in local flow direction $b_{\text{local}} = (u/(\partial u/\partial z))|_{\text{interface}}$ was assessed by fitting a linear function to the end of the velocity profile and extrapolating to $u = 0$ below the interface. When the FCS detection volume significantly enters a pillar or air, tracer concentration and excitation are undefined and hence measured velocities do not reflect the actual values. Therefore, velocities at positions $< 1\,\mu\text{m}$ from the interface have been discarded from the fit. Repeated measurements of the local slip length at the various positions showed a good repeatability with the maximum standard deviation occurring at point (0|6) ($\sigma_{b,\text{max.}} = 0.7\,\mu\text{m}$).

Local slip lengths (table 2(b)) vary significantly along the interface. In agreement with slip measurements on flat hydrophobic surfaces [2–9], the local slip almost vanishes at the pillar-water interface as within the accuracy of the measurements and the roughness due the PS particles. In between two pillars across the flow (0|6), b_{local} was largest with 14 µm. Since the shear stress at the interface only varies slightly (fig. 3), b_{local} mainly scales with u. The local slip distribution is reasonably symmetric, ((5|3) vs. (7|3) and (3|5) vs. (9|5)) confirming that the flow is in the low-Reynolds-number regime.

Furthermore, the experiments reveal an important property of the local slip length: it is anisotropic. Comparison of points (0|6) and (6|0), and (3|5) and (5|3), respectively, shows that the local slip is a function of the flow direction. While it is well known that the effective slip length may be anisotropic [39, 40], e.g. for grooved surfaces, the local slip length has typically so far been considered to be isotropic [17–28].

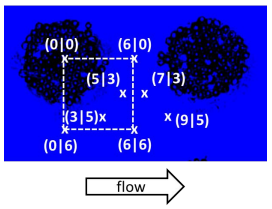

(a)

Point	b_{local} (µm)
(0|0)	0.2 ± 0.2
(6|0)	0.3 ± 0.2
(5|3)	2.4 ± 0.4
(7|3)	2.1 ± 0.3
(3|5)	7.1 ± 0.9
(9|5)	8.5 ± 1.4
(0|6)	14.0 ± 4.9
(6|6)	4.4 ± 0.5

(b)

FIG. 2: (a): Confocal image of the air-water interface (color = reflection) and the coated pillar tops. Measurement positions for the local slip length are indicated in a pillar-referred coordinate system. (b): FCS-measured values of the local slip length in the direction of flow. Uncertainties are calculated with respect to a given interface height.

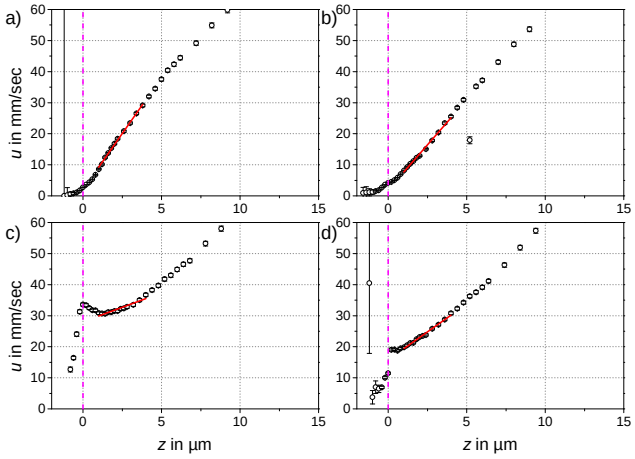

FIG. 3: Exemplary velocity profiles with fit for local slip length at points: a) (0|0), b) (6|0), c) (0|6), d) (6|6). Due to the detection volume crossing the interface, values do not represent the actual velocities for $z < 1\,\mu\text{m}$.

To further explore the local flow phenomena that determine the local slip, flow over a similar surface was calculated numerically. The model considers a 3D, periodic surface element. For simplification, the top of the pillar as well as the air-water interface were modeled to be flat, which is in reasonable accordance with the experimental observations. The net flux through the air layer is zero, accounting for the fact that in the experiment, the air layer is not connected to the environment but enclosed in the channel. In accordance with the symmetry of the experimental results, the Stokes equations were solved with the commercial finite-element solver Comsol

Multiphysics (for details, see SI).

For the flow of the water, the computations yield velocity profiles (fig. 4 (a)) that correspond well to the measured profiles. In addition, calculations also reveal the flow within the air layer. The air recirculates in a vortex behind the pillars and always has a backward facing component because of the air being enclosed in the channel. Due to mass conservation in the air layer the velocity at the interface is highest at the narrowest confinement between the pillars (0|6), illustrating the importance of the local flow field.

Above the pillar, the velocity profile in the water is approximately linear close to the interface. In contrast, above to the air-water interface, the velocity profile is nonlinear in proximity to the interface. For comparison with the experiments, where velocities were measured only for $z > 1\,\mu\text{m}$, we therefore define a virtual local slip length $b_{\text{virt.}} = (u/(\partial u/\partial z))|_{z=d} - d$. This is the apparent local slip length observed at the center of gravity $d = 2.3\,\mu\text{m}$ of the fit of the unevenly spaced experimental data (see SI).

The distribution of the numerically predicted local slip lengths in the direction of flow (fig. 4 (b)) is consistant with the the non-constant and anisotropic properties observed in the experiments. The distribution of the local slip length is determined by mass conservation in the air layer, leading to the slip length being largest at the point of narrowest confinement and low behind the pillar. Anisotropy is directly linked to the different flow patterns at the individual locations, e.g. strongly recirculating at (6|0) while flowing much less inhibited at (0|6).

In the region where the flow is not obstructed by the pillars (0|6), the experimental values and $b_{\text{virt.}}$ agree well. The local slip phenomena seem to be accurately represented by the hydrodynamics of the two fluids. In contrast, behind the pillars, velocity and local slip length are much smaller in the experiments than in the theoretical prediction. This indicates that further processes influence the slip on the microscopic level, for example interfacial impurities [16]. In a system with such high surface-to-volume ratio as studied here a complete absence of any surface impurity can not be guaranteed although we worked as clean as possible.

In order to clarify the role of fluid-fluid interface impurities, the sensitivity of the local slip length to the addition of a surfactant is investigated. As a surfactant, sodium 1-decanesulfonate (S-1DeS) (Sigma Aldrich) is employed, which at low concentrations, allows for comparatively small changes in the surface tension (66 mN/m at 0.1 cmc (critical micelle concentration 47mmol/l) and 50 mN/m at 0.4 cmc in water, Dataphysics DCAT11EC tensiometer). Hence, the water-air interface remains stable and close-to-flat as confirmed by confocal imaging.

The local slip length is clearly influenced by the presence of surfactants. Upon addition of even 0.1 cmc surfactant the flow is not only suppressed in the region in front of the pillars, but also at the remaining interface (table I). Due to the nature of the flow field, surfactants will first accumulate in front of the pillars and drive a backflow due to Marangoni forces. Consequently, concentration induced flows due to surface active substances lead to an effective no slip boundary condition. This is in line with our observation that there is hardly any flow at point (6|0). We expect that even small amounts of contaminations of the water-air interface can immobilize the motion at the interface and thereby negatively affect slippage at superhydrophobic surfaces. Also slippery surfaces that are based on an alternative lubricating fluid, like oil, could be affected. A similar behavior based on surfactant-concentration gradients is known to occur for bubbles [41]. Surface active substances are effectively always present, for example in the form of contaminations. They may be crucial for the design of applications as well as for the applicability of superhydrophobic surfaces.

Furthermore, we investigated the overall effective slip length b_{eff}. While flow close to a structured wall varies according to the local boundary conditions, these fluctuations die off far from the wall and the flow attains an average velocity profile. Therefore, the effective slip length is reflected in the velocity profile in the bulk of the chan-

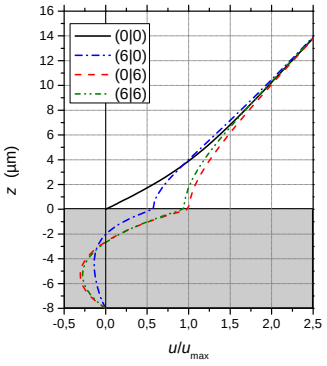

(a)

Point	$b_{\text{local, th}}$ (µm)	$b_{\text{virt.}}$ (µm)
(0|0)	0	0
(6|0)	56	4
(5|3) /		
(7|3)	77	7
(3|5) /		
(9|5)	89	12
(0|6)	91	15
(6|6)	99	15

(b)

FIG. 4: Numerically calculated flow phenomena close to the surface: (a) velocity profiles at selected positions; the velocity is normalized with the maximum velocity at the interface $u_{\max}$ (b) local slip length in the direction of flow $b_{\text{local, th}}$ and virtual local slip length $b_{\text{virt.}}$ observed at $z = cg$

Point	Local slip length (µm)	
	0.1 cmc S-1DeS	0.4 cmc S-1DeS
(0|0)	0.1 ± 0.2	-0.1 ± 0.2
(6|0)	0.2 ± 0.2	0.4 ± 0.2
(0|6)	5.3 ± 1.0	4.6 ± 0.9
(6|6)	3.9 ± 0.5	3.2 ± 0.8

TABLE I: Local slip length under the influence of sodium 1-decanesulfonate acting as a surfactant

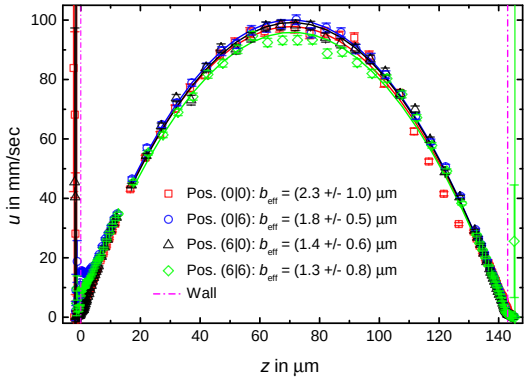

FIG. 5: FCS-measured velocity profiles across the channel with parabolic fit

nel. For the present channel geometry, where the pillar period is much smaller than the channel height and the channel height than its width, the average velocity profile is parabolic with a no slip condition at the unstructured, hydrophilic, lower wall and an effective slip at the superhydrophobic upper wall. The effective slip length was determined by recording velocity profiles across the entire channel and fitting them to a theoretical parabolic profile. A region of the order of the pillar period was excluded from the fit, making sure that the changes due to the varying wall structure have died off. For consistency, measurements of the effective slip length are performed at various positions (fig. 5). On average, we measured an effective slip length of $b_{\text{eff}} = 1.7 \pm 0.7\,\mu\text{m}$.

In the numerical model, the effective slip length $b_{\text{eff, th}}$ was obtained by matching the computed flow far from the structured wall with the theoretical profile for a flow with an effective slip length at the wall. With $b_{\text{eff, th}} = 4\,\mu\text{m}$, the theoretical value is about 2.5 times larger than the measured one. Since the theoretical model does not consider any influence of interface contaminations, the numerical value should be larger than the experimental one. Still, the experimental and numerical values for the effective slip length are closer to each other than the corresponding comparison of the local values would suggest (tables 2(b) and 4(b)). This stems from the fact that the characteristic local slip length of a classic superhydrophobic surface is quite large. With increasing local slip length, the effective slip length saturates towards the effective slip length of a corresponding surface with infinite local slip being assumed at the air-water interfaces, as long as the slipping-interface fraction is not too high and the stress at the air-water interface is not dominated by the surface topography, e.g. for shallow surfaces structures [29]. For the present surface, this limiting value was numerically calculated to be $4.3\,\mu\text{m}$. With respect to the measured effective slip length, the effect of saturation starts to become noticeable, but there is still an influence of the surface topography.

In this letter, we investigated the hydrodynamics of slippage at a microstructured surface in the Cassie state both experimentally by FCS measurements as well as theoretically by numerical calculations. We showed that local and effective slippage at surfaces can be explained by the local hydrodynamics of the air connected to the aqueous medium. The local flow pattern is influenced by the surface topography and surfactants adhering to the air-water interface and inducing Marangoni flows. Overall, this leads to a finite, non-constant and anisotropic distribution of the local slip length. Hence, not only the effective slip length but also the local slip length of such surfaces is anisotropic. These properties of the local slip length provide a path to appropriate modeling and hence to the physical understanding of superhydrophobic and related surfaces. Since current theoretical models use an isotropic, infinite or constant finite local slip length, it has to be evaluated to what extend such simple assumptions may reasonably be employed for the description of superhydrophobic or slippery surfaces. As we discussed in the context of the effective slip length, there are surfaces exhibiting a large local slip length, whose effective slip length is not very sensitive to changes in the local properties. With respect to the purely global, effective behavior of the flow, traditional models based on an infinite or isotropic local slip may consequently lead to similar results for the effective slip length or the overall drag despite the fact that the local processes are not well captured. If surface active substances regionally or generally block the motion in the lubricating layer and thereby significantly reduce the local slip length, new models are required, that take into account the properties of the local slip length. The same applies to surfaces with a small local slip length, e.g. due to a high viscosity of the lubricating medium, or when the geometry of the surface has a significant influence on the flow field close to the air-water interface. Apart from the global flow behavior, the correct modeling of local flow behavior relies on correct assumptions for the local slip length. This may for example be important for turbulent flow over slippery surfaces. With increasing Reynolds numbers, the vortices forming in the air should become asymmetric, leading to a different flow field and a different slip length distributions. To properly describe such cases, further investigations are needed.

The authors thank Lena Mammen and Noemí Encinas García for the preparation of the pillars and Franziska Henrich for the surface tension measurements of S-1DeS. We also thank the Polymer Theory Group at MPIP Mainz for access to the cluster computing facilities. Financial support from ERC for the advanced grant 340391-SUPRO is gratefully acknowledged.

* schoenecker@mpip-mainz.mpg.de

[1] M. Navier, Mémoires de l'Académie royale des Sciences de l'Institut de France **6**, 389 (1823).

[2] R. Pit, H. Hervet, and L. Léger, Tribology Letters **7**, 147 (1999).

[3] J. Baudry, E. Charlaix, A. Tonck, and D. Mazuyer, Langmuir **17**, 5232 (2001).

[4] V. S. J. Craig, C. Neto, and D. R. M. Williams, Physical Review Letters **87**, 054504 (2001).

[5] E. Bonaccurso, M. Kappl, and H.-J. Butt, Physical Review Letters **88**, 076103 (2002).

[6] C. Cottin-Bizonne, B. Cross, A. Steinberger, and E. Charlaix, Physical Review Letters **94**, 056102 (2005).

[7] P. Joseph and P. Tabeling, Phys. Rev. E **71**, 035303 (2005).

[8] D. Lasne, A. Maali, Y. Amarouchene, L. Cognet, B. Lounis, and H. Kellay, Phys. Rev. Lett. **100**, 214502 (2008).

[9] E. Lauga, M. P. Brenner, and H. A. Stone, in *Handbook of Experimental Fluid Dynamics*, edited by J. Foss, C. Tropea, and A. Yarin (Springer, 2005).

[10] E. Schnell, Journal of Applied Physics **27**, 1149 (1956).

[11] K. Watanabe, Y. Udagawa, and H. Udagawa, Journal of Fluid Mechanics **381**, 225 (1999).

[12] P. Tsai, A. M. Peters, C. Pirat, M. Wessling, R. G. H. Lammertink, and D. Lohse, Physics of Fluids **21**, 112002 (2009).

[13] G. McHale, N. J. Shirtcliffe, C. R. Evans, and M. I. Newton, Applied Physics Letters **94**, 064104 (2009).

[14] N. J. Shirtcliffe, G. McHale, M. I. Newton, and Y. Zhang, ACS Applied Materials & Interfaces **1**, 1316 (2009).

[15] D. Song, R. Daniello, and J. Rothstein, Experiments in Fluids **55**, 1783 (2014).

[16] G. Bolognesi, C. Cottin-Bizonne, and C. Pirat, Physics of Fluids **26**, 082004 (2014).

[17] E. Lauga and H. A. Stone, Journal of Fluid Mechanics **489**, 55 (2003).

[18] J. Davies, D. Maynes, B. W. Webb, and B. Woolford, Physics of Fluids **18**, 087110 (2006).

[19] M. Sbragaglia and A. Prosperetti, Physics of Fluids **19**, 043603 (2007).

[20] A. M. J. Davis and E. Lauga, Physics of Fluids **21**, 011701 (2009).

[21] D. Crowdy, Physics of Fluids **22**, 121703 (2010).

[22] A. M. J. Davis and E. Lauga, Journal of Fluid Mechanics **661**, 402 (2010).

[23] S. Türk, G. Daschiel, A. Stroh, Y. Hasegawa, and B. Frohnapfel, Journal of Fluid Mechanics **747**, 186 (2014).

[24] A. V. Belyaev and O. I. Vinogradova, Journal of Fluid Mechanics **652**, 489 (2010).

[25] A. V. Belyaev and O. I. Vinogradova, Physical Review Letters **107**, 098301 (2011).

[26] K. Kamrin, M. Z. Bazant, and H. A. Stone, Journal of Fluid Mechanics **658**, 409 (2010).

[27] E. S. Asmolov and O. I. Vinogradova, Journal of Fluid Mechanics **706**, 108 (2012).

[28] E. S. Asmolov, S. Schmieschek, J. Harting, and O. I. Vinogradova, Physical Review E **87**, 023005 (2013).

[29] C. Schönecker, T. Baier, and S. Hardt, Journal of Fluid Mechanics **740**, 168 (2014).

[30] L. Mammen, K. Bley, P. Papadopoulos, F. Schellenberger, N. Encinas, H.-J. Butt, C. K. Weiss, and D. Vollmer, Soft Matter **11**, 506 (2015).

[31] O. I. Vinogradova, K. Koynov, A. Best, and F. Feuillebois, Physical Review Letters **102**, 118302 (2009).

[32] S. Yordanov, A. Best, H.-J. Butt, and K. Koynov, Optics Express **17**, 21149 (2009).

[33] D. Magde, E. Elson, and W. W. Webb, Physical Review Letters **29**, 705 (1972).

[34] M. Gösch, H. Blom, J. Holm, T. Heino, and R. Rigler, Analytical Chemistry **72**, 3260 (2000).

[35] R. Rigler and E. Elson, eds., *Fluorescence Correlation Spectroscopy* (Springer, 2001).

[36] D. Lumma, A. Best, A. Gansen, F. Feuillebois, J. O. Rädler, and O. I. Vinogradova, Physical Review E **67**, 056313 (2003).

[37] K. Koynov and H.-J. Butt, Current Opinion in Colloid & Interface Science **17**, 377 (2012).

[38] D. Schaeffel, S. Yordanov, M. Schmelzeisen, T. Yamamoto, M. Kappl, R. Schmitz, B. Dünweg, H.-J. Butt, and K. Koynov, Physical Review E **87**, 051001 (2013).

[39] H. Stone, A. Stroock, and A. Ajdari, Annual Review of Fluid Mechanics **36**, 381 (2004).

[40] M. Z. Bazant and O. I. Vinogradova, Journal of Fluid Mechanics **613**, 125 (2008).

[41] V. G. Levich, *Physicochemical Hydrodynamics* (Prentice-Hall, 1962).